

# Satellite-Based Fire Progression Mapping: A Comprehensive Assessment for Large Fires in Northern California

Erica Scaduto , Bin Chen , and Yufang Jin 

**Abstract**—Satellite-based active fire (AF) products provide opportunities for constructing continuous fire progression maps, a critical dataset needed for improved fire behavior modeling and fire management. This study aims to investigate the geospatial interpolation techniques in mapping the daily fire progression and assess the accuracy of the derived maps from multisensor AF products. We focused on 42 large wildfires greater than 5000 acres in Northern California from 2017 to 2018, where the USDA Forest Service National Infrared Operations (NIROPS) daily fire perimeters were available for the comparison. The standard AF products from the moderate resolution imaging spectroradiometer (MODIS), the visible infrared imaging radiometer suite (VIIRS), and the combined products were used as inputs. We found that the estimated fire progression areas generated by the natural neighbor method with the combined MODIS and VIIRS AF input layers performed the best, with  $R^2$  of  $0.7 \pm 0.31$  and RMSE of  $1.25 \pm 1.21$  ( $10^3$  acres) at a daily time scale; the accuracy was higher when assessed at a two-day rolling window, e.g.,  $R^2$  of  $0.83 \pm 0.20$  and RMSE of  $0.74 \pm 0.94$  ( $10^3$  acres). A relatively higher spatial accuracy was found using the 375 m VIIRS AF product as inputs, with a kappa score of 0.55 and an overall accuracy score of 0.59, when interpolated with the natural neighbor method. Furthermore, the locational pixel-based comparison showed 61% matched to a single day and an additional 25% explained within  $\pm 1$  day of the estimation, revealing greater confidence in fire progression estimation at a two-day moving time interval. This study demonstrated the efficacy and potential improvements of daily fire progression mapping at local and regional scales.

**Index Terms**—Fire behavior, geospatial, moderate resolution imaging spectroradiometer (MODIS), northern California, visible infrared imaging radiometer suite (VIIRS), wildfire.

## I. INTRODUCTION

THE frequency and intensity of wildfires have been increasing in the western United States over the past few decades, raising urgent needs in disentangling the drivers of this shifting fire regime [1], [2]. The accumulation of fuels, coupled with the joint effects of warming temperatures and precipitation

anomalies, as seen in California's most recent episode of acute drought [3], and strong winds, has been associated with the intensified wildfire behavior in recent years.

Human-related drivers, such as population growth, expansion of human settlement, forest management decisions, and cultural perceptions of fires, have also been thought to magnify the destructive nature of wildfires [4]. Forest management policies have removed frequent and often nonlethal fires by implementing fire suppression efforts since the late 19th century, resulting in the alteration of fuel dynamics and increased susceptibility of high-intensity fires [2], [5], [6]. Therefore, the efficient and more accurate methods of monitoring and simulating fire spread are crucial for supporting near real time, on-the-ground aid for firefighting, and for providing the basis for future fire and forest management efforts.

To support wildfire suppression and tactical fire management across the United States, the USDA Forest Service National Infrared Operations (NIROPS) acquire high spatial resolution, night-time aerial thermal infrared (IR) imagery at an overall resolution of 6.3 m, upon requests by an agency and interagency wildfire management communities [7]. The tactical scale daily fire perimeter maps are then generated by IR imagery interpreters. These products have benefited the incident command teams tremendously by increasing their situational awareness and informing their on-the-ground decision making. Some studies have also relied on these daily fire progression maps to understand the influence of weather and other biophysical factors on fire behavior [8], [9]. However, aerial data acquisition is expensive, and thus, these maps are still only available for limited fire incidences. Logistical challenges in airborne-based data acquisition, including the limitation of resources and adherence to safety concerns during high winds and peak fire activity, also impose inherent complications for the dataset. Furthermore, due to the finite number of how many fires can be mapped on any given day, prioritizations were often made toward generating the maps for fires that pose risks to human life and infrastructure, and only a small number of fires were mapped in extremely remote locations.

The satellite remote sensing, on the other hand, has the capability for consistent monitoring of wildfires across the globe, including near real-time hotspot detection from thermal sensors [10], [11] and postfire burned area mapping from optical sensors [12]. The launch of Terra with the moderate resolution imaging spectroradiometer (MODIS) in 1999, and Aqua shortly

Manuscript received May 26, 2020; revised July 21, 2020; accepted August 18, 2020. Date of publication August 25, 2020; date of current version September 16, 2020. This work was supported in part by the UC National Laboratory Fees Research Program, in part by California's Strategic Growth Council (SGC) Climate Change Research Program to the Center for Ecosystem Climate Solutions at UC Irvine, in part by the USGS's America View Grant, and in part by the NASA's California Space Grant Consortium. (Corresponding author: Erica Scaduto.)

The authors are with the Department of Land, Air, Water Resources, University of California, Davis, Davis, CA 95616 USA (e-mail: escaduto@ucdavis.edu; bch@ucdavis.edu; yujin@ucdavis.edu).

Digital Object Identifier 10.1109/JSTARS.2020.3019261

after, has significantly advanced the capabilities of active fire (AF) detection, with four overpasses a day and the specific configuration of two 1 km thermal channels centered at 4 and 11- $\mu\text{m}$  to detect hotspots [13]. The MODIS thermal anomaly products take advantage of the differential response between 4 and 11- $\mu\text{m}$  brightness temperatures ( $BT_4$  and  $BT_{11}$ ) [14], [15]. The fire detection algorithm first identifies potential fire pixels based on a threshold test of  $BT_4$  and  $BT_4 - BT_{11}$  difference.  $BT_4$  is particularly useful due to its increased sensitivity toward the flames at 1000 K and smoldering at 600 K [16], [17]. The characterization of neighboring nonfire background pixels is then quantified using a moving window. The final identification of fire pixels is determined based on a suite of contextual tests that offer the detection of smaller and/or cooler fires, largely based on the degree of departure of potential fire pixel from its nonfire background [15], [18].

Further improvements to the algorithm have been made to produce the most recent collection 6 (C6) MOD14 (Terra) and MYD15 (Aqua) AF products [18]. Most noticeably, the thresholds for the preliminary identification of potential fire pixels are now set dynamically for each position of the MODIS scan, which helps compensate for local variations [18]. Additional refinements also reduce omission errors over large fires and false alarm rates in certain regions, with an overall daytime commission error of 1.2% compared with 2.4% in collection 5 [18].

Global area burned products have also been produced based on the rapid change in daily reflectance after fires at 500 m resolution (MCD45A1), providing the approximate date of burning and the spatial extent of recent fires [19]. Significant improvement has been made to combine the thermal anomaly and changes in the optical reflectance for area burned mapping (MCD64A1) [19]–[21]. A preliminary evaluation of the most recent collection (C6) MCD64A1 showed that 44% of the burned grid cells was detected on the same day of AF detection and 68% within two days, globally [19]. However, there still exist gaps in terms of temporal consistency and the availability of spatially complete daily fire perimeters, due to the obscuration of the ground by the cloud and smoke, and the challenge to detect smaller and cooler hotspots.

The visible infrared imaging radiometer suite (VIIRS) aboard the Suomi National Polar Partnership, launched in 2011, further provides unprecedented fire detection capabilities due to its finer spatial resolution, higher signal-to-noise ratio, dual-gain high-saturation channels, and a notable reduction of pixel growth off-nadir [22]. The standard VIIRS AF products (VAFPs) use thermal anomaly detection directly based on the MODIS collection 6 AF [23], [24]. VIIRS holds an advantage over other legacy instruments specifically for detecting smaller and cooler fires [24]. For example, both MODIS and VIIRS are whiskbroom sensors, with issues in systematic omissions and duplication in the detection based on scan angles [14], [25]. However, VIIRS off-nadir pixel growth is limited to up to four times that of nadir pixels, mainly due to the asymmetrical detector and unique sample aggregation scheme, much smaller than a factor of ten from MODIS [24], [26]. This preservation of off-nadir pixels

results in better detectability of low-energy fires at off-nadir view.

The increased reliability in satellite-based fire detection products overtime has lead the forest management to acknowledge its merit and utility in fire monitoring and firefighting efforts. The near real-time versions of the MODIS and VAFPs have been distributed to forest managers and stakeholders within 3 h of the satellite observation via the fire information for the resource management system [27], [28]. However, hotspot detection is still constrained by satellite overpass times, while cloud and smoke cover further limits the number of clear scenes available [14], [25].

Fire progression maps at finer temporal and spatial scales are needed in order to examine an important aspect of wildfire behaviors, fire spread, in relation to weather and local environmental conditions, such as fuels and topographical conditions [8], [9]. A robust algorithm and workflow of producing continuous fire perimeter maps from consistent publicly available datasets can further help to calibrate process-based fire behavior models. In response to this data need, a few studies have explored the traditional geostatistical interpolation methods, i.e., nearest neighbor, ordinary kriging, and inverse distance weighted (IDW), to derive the continuous maps of daily fire progression from standard MODIS thermal anomaly products [29], [30]. The derived daily fire perimeters were shown to have a relatively good agreement with the reference fire perimeters curated by federal and multiagency groups. For instance, the ordinary kriging method was shown to correctly map 73% of pixels at daily intervals for nine large wildland fires across the U.S. [30]. However, the use of coarser-resolution MODIS AF products as the only input limits the accuracy and also the scope to very large wildland fires, typically greater than 3000 hectares (30 km<sup>2</sup>). Likewise, due to the limited sample size across fire regimes, there is no additional investigation into the model accuracies that may arise in certain environmental conditions and fire characteristics. The application of the previously studied interpolation methods may, therefore, result in variable spatiotemporal uncertainties.

This study, therefore, aims to evaluate the detection efficacy of the MODIS and VAFPs, investigate the ability of various interpolation techniques for mapping daily fire progression based on the AF input layers from different sensors, and develop a workflow to create a geospatial database of daily fire perimeter estimation, both retrospectively and in near real time, for fire behavior and fire ecology research. By assessing the methodologies and sensors that are well-suited for daily fire progression estimation, this study is expected to optimize and ultimately improve the daily fire perimeter datasets to aid in the historical and predictive fire behavior analysis and ultimately provide insights for management strategies.

## II. MATERIALS AND METHODS

### A. Study Area

This study focuses on the nonagricultural lands in Northern California, including Monterrey, Kings, Tulare, and Mono counties (see Fig. 1). It encompasses six Level-III ecoregions:

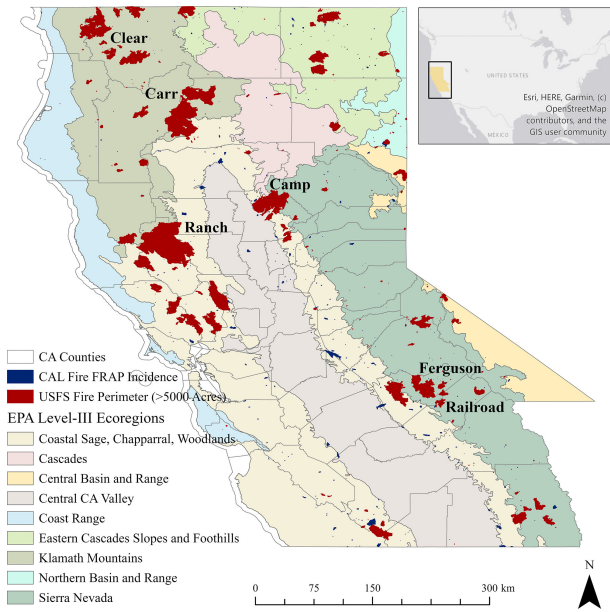


Fig. 1. Map of the study region. The area burned by 2017 to 2018 wildfires greater than 5000 acres in Northern California, overlaid over the county lines and EPA ecoregion map. Six example fires for illustrative purposes throughout the article are labeled, including Camp, Carr, Clear, Ferguson, Railroad, and Ranch fires. Other fires recorded by the Cal Fire FRAP database in these two years are also shown in blue.

Klamath mountain/Coastal ranges, Central Foothills/Coastal Mountains, Sierra Nevada, East Cascades Foothill, Central basin and range, and Cascades.<sup>1</sup> The majority of the region is characterized by a Mediterranean climate with hot, dry summers and cool, wet winters. The landscape is dominated by coniferous forests, oak woodlands, lower and upper montane, subalpine, and grassland vegetation types. Specifically, the Klamath Mountain/Coastal Range ecoregion's notable vegetation includes chaparral and oak woodlands, grasslands in lower elevations, and pines, such as colter pine in higher elevations [31]. In the Sierra Nevada ecoregion, the vegetation ranges from ponderosa pine, douglas fir, sierra juniper at lower elevations, and conifers at higher, subalpine conditions. Dominant vegetation types for Coastal Mountains within lower-lying mountains and hills include several conifer species such as redwood, douglas fir, and sitka spruce, in addition to some cultivated lands within the parts of Salinas, Napa, and Sonoma [31].

Although many ecosystems in the western U.S. are dependent upon recurring low to moderate intensity fires, shifting patterns of precipitation, temperature, and fuel conditions, coupled with wildland management practices, continue to heighten the frequency of high severity fires in the region. In 2017 and 2018, records were undeniably broken within two consecutive wildfire seasons that devastated California. Dozens of wildfires spread across Northern California in October 2017, one of which was named the most destructive fire on record, destroying at least 5643 structures [32]. However, on November 8, 2018, Campfire, causing at least 86 casualties, destroying 18 804 structures, and

burning over 150 000 acres, became the state's deadliest and destructive fire, superseding the records set by fires from the years prior [33]. Therefore, in an effort to aid in the subsequent fire research across the region, we here focus on wildfires across Northern California larger than 5000 acres (20.23 km<sup>2</sup>) from 2017 to 2018, where the daily fire perimeters were available from NIROPS. The 42 fires are partly a total of 373 fires in 2017 and 220 fires in 2018 according to the FRAP fire perimeter dataset<sup>2</sup> (see Fig. 1).

## B. AF Data

We used the standard AF point data generated from MODIS [18], VIIRS [24], and a combination layer, as the input to map the daily fire progression. The level 2 MODIS 1 km AF products (MOD14 and MYD14), from Terra (10:30 and 22:30 Equatorial local overpass time) and Aqua (13:30 and 01:30 Equatorial local overpass time), provide the geolocation of fire hotspots, fire mask, detection confidence, and fire radiative power since 2002 (last accessed on 24 April, 2019) [18]. The fire detection algorithm takes advantage of the radiances observed in BT<sub>4</sub> and BT<sub>11</sub> channels after eliminating the cloud and water cover [19]. Potential fire pixels are screened through several tests based on thresholds and contextual comparisons between neighboring nonburning background values. It is noted that the probability of the MODIS AF algorithm to detect a fire that is 100 m<sup>2</sup> is 50% during the ideal conditions with the absence of obscuration from clouds, thick aerosols, and or tree canopy [14]. Uncertainties in both MOD14 and MYD14 products have been well accounted for by various comparisons between the high-resolution reference AF datasets and have reached various levels of maturity in the validation [14], [34].

The VIIRS instrument onboard the Suomi National Polar-Orbiting Partnership satellite is considered the next generation of MODIS, providing the global coverage every 12 h crossing over the equator twice daily at 13:30 and 1:30 Equatorial local overpass times. VIIRS acquires both 375 m imagery bands (*I*-bands) that are comprised of five single-gain channels from the visible to thermal IR spectral region and 750 m moderate-resolution bands (*M*-bands) [24]. Relative to the VIIRS *M*-Band 750 m AF data product, we here used the standard level 2 VIIRS *I*-band AF product (VNP14IMG) (last accessed on 24 April 2019) due to its higher spatial resolution and improved fidelity in fire mapping. VNP14IMG builds upon the legacy MODIS multispectral algorithm, where the channel *I*<sub>4</sub> (3.44–3.93 μm) is the primary band compared with the *I*<sub>5</sub> (10.5–12.4 μm). The remaining *I*-bands (*I*<sub>1</sub>, *I*<sub>2</sub>, and *I*<sub>3</sub>) are used for the daytime portion of the operation to aid in reducing the noise from clouds, sun glint, and water body [24].

Compared with the VIIRS M13 and MODIS 21 and 22 bands used in baseline AF products, the *I*<sub>4</sub> channel has a lower saturation temperature of 367 K [24]. Consequently, this results in the frequent pixel saturation for large and/or intense fires, and potential reduction in differentiating between fires and bright surfaces [24], [26]. To best accommodate for discrepancies when taking advantage of higher spatial resolution channels,

<sup>1</sup>[Online]. Available: <ftp://newftp.epa.gov/EPADDataCommons/ORD/Ecoregions/ca/>

<sup>2</sup>[Online]. Available: <https://frap.fire.ca.gov/mapping/gis-data/>

VNP14IMG incorporates a few modifications that offer better response over subpixel AFs [24]. Overall, initial assessments show the improved net performance of *I*-band fire products, with a higher level of agreement to airborne and Landsat-8 AF data [24], [35].

For the purposes of comparison and combining the MODIS and VIIRS AF products, we resampled the MODIS 1 km AF products to 375 m resolution (see Fig. 8). The resampling was performed for each unique day of a fire event and then combined to one raster layer for each individual fire. To minimize data redundancy from reburned areas at later timestamps, we removed overlapping points, prioritizing the earliest days of the burn. The conversion of 1 km to a common higher spatial resolution allowed for an increase in the number of neighboring AF points, which was particularly helpful in the case of smaller fires and made the results between two sensors more comparable. We further integrated the MODIS and VAFPs into a combined layer, in order to test the capability of mapping fire progression when using both complementary sensors when in operation.

Due to the similar orbiting and afternoon overpassing time of Suomi, and Aqua satellites, some AFs may be detected by both sensors, leading to redundancy. We, therefore, identified the redundant detection from both sensors when the hotspots were detected within 20 min and located 200 m from each other and removed overlapping fire presence points from the upscaled MODIS points. This helped offset any bias from impartial weights across the dataset.

### C. Daily Fire Perimeter Data

Daily fire perimeters were only available for certain large fires and are typically used to provide near real-time information for fire managers. We here obtained all available data for 2017–2018 large fires within our study region, through the U.S. Geological Services Geospatial MultiAgency Coordination file server via,<sup>3</sup> which reflect the cumulative area burned since the initial ignition. The daily fire perimeters were created by the interpretation of high-resolution night-time IR imagery from the USDA Forest Service National IR Operations (NIROPS) by the trained fire personnel. For each requested incident, the NIROPS team develops flight plans to fly their airborne IR sensors at night to take advantage of the contrasts in the temperature. The acquisition time for the daily perimeters varies but is mostly between 21:00 to 03:00 local time, after integrating necessary preprocessing and product creation steps. In some incidences, there are multiple reports within a day and we here only used the latest time of the day to represent the furthest extent of the burn at daily intervals.

Furthermore, in various instances there have been inconsistencies in the NIROPS released fire perimeter reports that have led to one-off edits. For example, an erroneous representation of the Natchez fire perimeter on July 28, 2018 02:05 was found, which resulted in the manual removal of the extraneous perimeter. The additional instances of varying perimeter representation were identified where NIROPS geometries were overgeneralized but

TABLE I  
MODEL PARAMETERS AND SEMIVARIOGRAM CHARACTERISTICS

Fire	Combined			VIIRS			MODIS		
	Sill	Range	$C_0$	Sill	Range	$C_0$	Sill	Range	$C_0$
Camp	15.21	0.45	2.94	16.65	0.44	2.56	12.94	0.45	2.95
Carr	64.46	0.28	0.00	66.14	0.29	0.00	58.08	0.28	0.00
Clear	15.54	0.03	0.39	15.01	0.02	0.00	16.26	0.03	0.00
Ferguson	65.79	0.16	0.00	63.14	0.16	0.00	67.07	0.16	0.00
Railroad	9.96	0.12	1.09	9.80	0.10	1.06	9.22	0.13	0.96
Ranch	140.91	0.42	0.00	163.12	0.42	0.00	110.71	0.43	0.00

updated at a later time. Therefore, to reduce errors from over- and underdrawn perimeters, these layers were carefully evaluated for any obvious errors and updated accordingly.

### D. Geostatistical Methods

AF products from MODIS and VIIRS provide discontinuous data points, with attributes of detection time, location, confidence, and intensity of flames [19], [24]. In order to derive a spatially continuous fire progression map at a daily interval, we here examined various geospatial interpolation methods, including ordinary kriging (KRG) [30], IDW [7], natural neighbor (NAT) [36], and empirical Bayesian kriging (EBK) [38]. For each individual fire, we extracted the AF data points, 48 h before and after the respective start, and end dates based on the USFS fire incidence records. The interpolation was done over the timestamps of detected AF grids from each input layer, e.g., MODIS, VIIRS, and combined layer, respectively. We further gridded the outputs to 375-m resolution, masked to the final USFS fire incidence perimeter, and floored to the nearest Julian day of the year (JDOY) to enable intercomparison among all products. In an effort to increase the consistency among the methodology and create a reproducible workflow, all data manipulations and processing were performed using geoprocessing techniques within ESRI's ArcGIS Pro toolbox. In addition, parameters for each method were adjusted to ensure reasonable accuracy across the majority of fires in the region.

Ordinary kriging (KRG) is a widely known geostatistical interpolation technique, originally used to estimate metal concentrations but since then has been used to estimate a broad range of environmental variables, such as precipitation, elevation, and air temperature [38], [39], [42]. It calculates values at unknown locations based on the statistical relationships between attributes at nearby known locations. For each fire, the semivariogram was calculated, which describes the spatial variability between each AF data point in relation to the distance from neighboring points. The weights are determined by calculating the covariance among the sample AF points among each other and the unknown by fitting a spherical model to the semivariogram curve. The kriging parameters, including the range, sill, and nuggets, for each of the fires differed across the study region, as observed in Table I. For example, fires, such as Carr, Ranch, and Ferguson, did not exhibit a nugget effect; however, some fires, including Camp and Clear, had nugget values larger than 0 days<sup>2</sup>. The sill and range values varied across each fire. According to Table I,

<sup>3</sup>[Online]. Available: <https://rmgsc.cr.usgs.gov/outgoing/GeoMAC/> (last accessed on 24 April 2019)

sill values were from 9 to 140.91 days<sup>2</sup>, while range values were between 0.03 and 0.45.

The IDW method is another popular approach to predict the attributes of unsampled locations from control points [29]. Unlike ordinary kriging, IDW determines its weights based on the inverse distance function, where the proximity of neighboring points to the unsampled locations and estimated values is highly contingent. The deterministic properties of IDW and the arbitrary choice in defining a neighborhood can be problematic for the prediction of the fire progression across various fire characteristics (duration, area, etc.). For this study, we selected the power coefficient  $p$  of 2, whereas when  $p$  increases the weights of distant points to the predicted location diminishes. In addition, we also used the variable-search-radius class to ensure a reasonable amount of flexibility in the model. Hence, the definition of neighborhood search was defined as reaching a minimum number of eight AF points and/or a maximum distance of 2 km.

The natural neighbor interpolation method takes the weighted average over the attributes of nearby known locations [36]. Specifically, it uses the Voronoi tessellation to calculate Sibson weights, for each unknown location, based on the areal proportion of overlapping the Voronoi polygons when the unknown point is inserted and then removed from the tessellation. In other words, the weights are determined by the degree of influence of the surrounding area to the location to be interpolated. This method thus has the advantage over simpler methods that place equal weights based solely on the distance of neighboring points.

In the classical kriging methods, such as ordinary kriging (KRG), the model assumes that the estimated semivariogram is the true semivariogram of the observed data [37]. On the other hand, EBK allows for an iterative simulation of the semivariogram, where with each repetition a new set of values is estimated at the input locations thus accounting for uncertainties. These new values are then used to create a semivariogram model to obtain weights for the final predictions [41]. Unlike the classical methods, the spectrum of semivariograms allows a distribution of possible values, which are then used to create the simulated surface. Although still fairly new, EBK shows promising applications and has already been successful in the determination of radiation contamination level, and in benthic mapping [41].

#### E. Temporal Accuracy Assessment

We quantified the accuracy of the original AF products and the interpolated daily fire progression outputs, in terms of capturing the daily area burned, by comparing with the NIROPS derived daily fire perimeter data at the same timestamp. Since the interpolated results reflect continuous time during the AF occurrence over each pixel, they were floored to the nearest day and aggregated in a way to match the discrete dates when the NIROPS derived perimeters were reported. For example, considering a fire with perimeters mapped on JDOY 314 and then again on 316 by the NIROPS team; the JDOY 316 perimeter from the reference contained the areas potentially burned on JDOY 315, and comparisons were thus made with the interpolated results aggregated for 315 and 316. Furthermore, if a reported

fire perimeter was recorded prior to 04:00 h, then the JDOY were changed to reflect the latest extent of the previous day based on the assumption that the majority of the fire burned the previous evening.

We made the comparisons for each individual fire and each individual reported day and then calculated the  $R^2$  and root-mean-square error (RMSE) between the observed and predicted areas of burn over all fires. The rolling  $R^2$  and RMSE values were also computed with a two-day moving window to account for general discrepancies between the timing of the fire reporting, and overpass time of satellite sensors.

#### F. Spatial Accuracy Assessment

To assess how well the interpolated daily fire progression maps match the USFS daily fire perimeter spatially, we made the pixel-based map-to-map comparisons on a daily time scale. USFS fire incident perimeters were rasterized to 375 m to be compatible with the interpolated results. The proportion of areas with matching and non-matching days was calculated by difference. Additionally, we used the confusion matrix approach to quantify the overall accuracy and Cohen's kappa coefficient. For each fire, due to a large amount of data, we randomly chose 1000 samples of USFS fire progression map as the ground truth to generate the confusion matrix; this randomization process was repeated  $100\times$  to increase the robustness of the assessment. For the purposes of all statistical analysis and comparison, we here used the scikit-learn library via python.<sup>4</sup>

To examine if the uncertainties of fire progression mapping vary with ecoregions and fire characteristics, comparison results were also summarized over key ecoregions and fire size [42]–[44].

### III. RESULTS

#### A. AF Detection Assessment

AF detection products were found to be consistent in identifying the general direction of fire spread and locations of AF fronts during designated overpass times. The Campfire was reported to start from the PG&E power transmission lines near Poe Dam, in Butte County around 06:15 am Pacific standard time (PST) on November 8, 2018 [45]. Both MODIS and VIIRS detected hotspots, located a few miles east of the dam, during their respective morning overpassing time, e.g., 10:14 PST (Terra), 11:52 PST (Terra and VIIRS), and 13:31 PST (Aqua) (see Fig. 2).

As shown by both satellite- and USFS-based daily fire perimeters, the fire spread quickly toward the southwest direction during the first two days, due to the combination of hot gusting winds and dry fuel loads. During the first two days, the USFS reported fire perimeters with 108 838 acres of burned area. The MODIS AF products detected approximately 56 748 acres (402 individual points at 1 km) and the VIIRS AF products detected around 40 046 acres (1769 points at 375 m). Detection omissions from both MODIS and VIIRS AF products were predominantly observed in the southwestern direction of fire perimeters during this period (see Figs. 2 and 3). This bias may be the result of

<sup>4</sup>[Online]. Available: <https://scikit-learn.org>

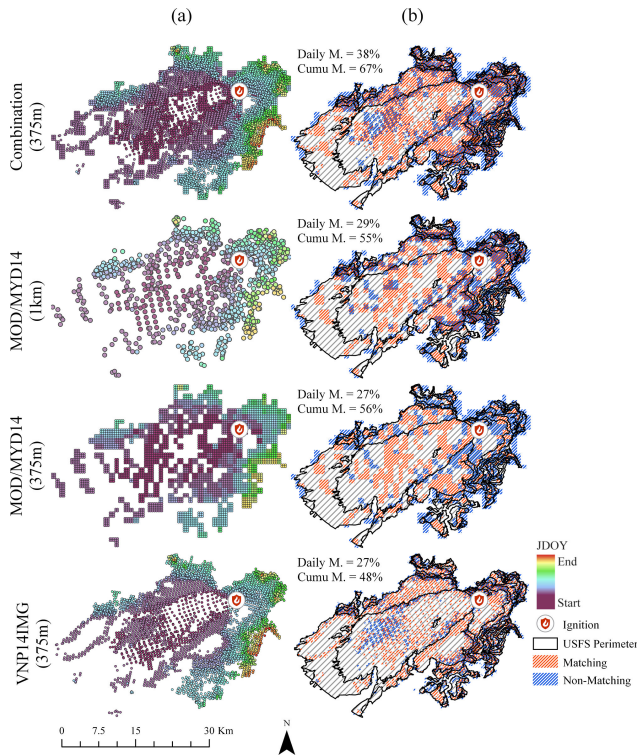


Fig. 2. Examples of the vector and gridded AF hotspots for the Campfire detected by combined VIIRS and MODIS, MODIS Terra and Aqua (1 km), MODIS (resampled at 375 m), and VIIRS from top to bottom. (a) Original AF products of daily fire progression. (b) Proportion of matching (red), nonmatching (blue), and omission (gray) areas between the satellite-based detection and USFS reported fire perimeters (shown as polygons) for a particular day (daily  $M$ ).

steep terrain (i.e., heterogeneous ridges and canyons), high rate of fire spread, and lower intensity flames during overpass times.

We also identified that there were discrepancies in the detected days at a daily time scale, where small pockets within a particular USFS daily perimeter were detected as AFs at later days by the satellite-based AF products [as shown in blue in Fig. 2(b)]. This could be attributed to the fact that fires burning with higher intensity flames would be reported in subsequent days. In terms of the overall proportion of daily matched areas for Campfire, MODIS (29%) and VIIRS (27%) showed relatively similar results over the entire duration [see Figs. 2(b) and 3]. Specifically, VIIRS was more sensitive to capture AFs over smaller areas with much refined spatial details, while the larger pixel size of MODIS made it more appropriate to encompass a wider area and its estimates were more comparable to the USFS perimeters, especially for large fires. Cumulatively, without considering the mismatch in detection dates, MODIS AF products captured 55% and VIIRS 48% of matched areas for Campfire [see Fig. 2(b)].

The proportion of matched areas between the MODIS and VIIRS AF detections was quite similar. However, in general, more early/late detections were found using MODIS AFs, while certain underestimates were observed using VIIRS AF products at daily intervals [see Figs. 2 and 3]. This difference in detection can mainly be attributed to the sensor's spatiotemporal properties, including the number and timing of daily overpasses as well as the overall sensitivity toward the thermal anomaly detection.

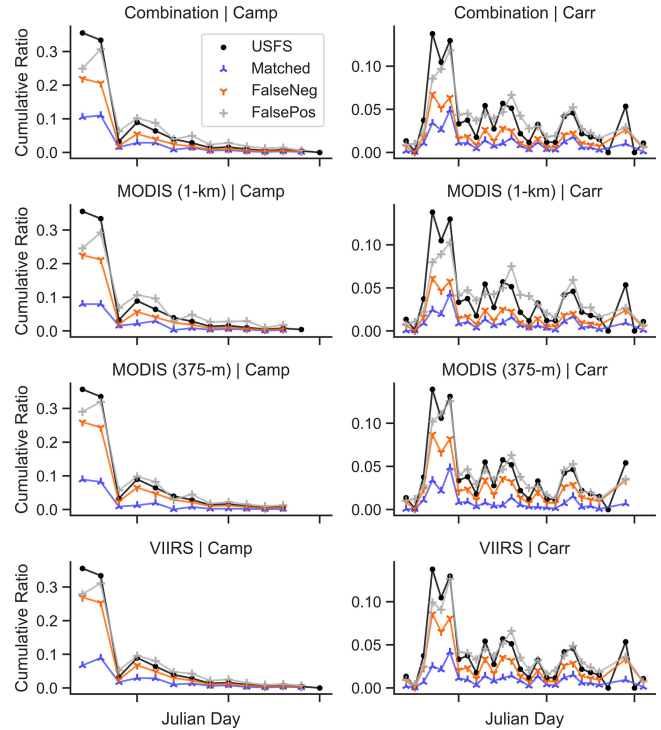


Fig. 3. Time-series-stacked proportions for the Camp and Carr fires (column) based on input layers (row). USFS reported burned area (black), matched (blue), and false negative (orange) cumulative ratios. False positive (gray) represents the proportion of early/late detected areas that fell outside of the USFS perimeter on the reported day.

TABLE II  
AREAL PROPORTION OF MATCHED SATELLITE-DERIVED AF DETECTIONS WITH USFS PERIMETERS

Layer	Daily Matching	Daily False Negative	Cumulative Matching
	Mean $\pm$ SD*	Mean $\pm$ SD	Mean $\pm$ SD
Combination	0.35 $\pm$ 0.11	0.23 $\pm$ 0.11	0.84 $\pm$ 0.12
MODIS (1-km)	0.28 $\pm$ 0.08	0.31 $\pm$ 0.15	0.72 $\pm$ 0.17
MODIS (375-m)	0.27 $\pm$ 0.09	0.40 $\pm$ 0.11	0.71 $\pm$ 0.17
VIIRS	0.31 $\pm$ 0.1	0.41 $\pm$ 0.17	0.65 $\pm$ 0.19

\*SD refers to the standard deviation.

Among all 42 fires, compared with the reference extent of USFS fire perimeters (see Table II), we found that the MODIS AF detection had a higher cumulative detection rate ( $0.72 \pm 0.17$ ) than that of VIIRS ( $0.65 \pm 0.19$ ). Similarly, by averaging over all individual detection days, the daily underestimate rate for MODIS ( $0.31 \pm 0.15$ ) was lower than that of VIIRS ( $0.41 \pm 0.17$ ), which might be due to the fact that MODIS's relatively larger pixel size allowed for a larger coverage of fire incidents, and capturing pre, post, and actively burning areas. In contrast, the aggregation over a larger extent consequently would reduce the spatial sensitivity and coherence, which was observed by the lower daily matching rate for MODIS ( $0.28 \pm 0.082$ ) compared with VIIRS ( $0.31 \pm 0.1$ ). Overall, the combination

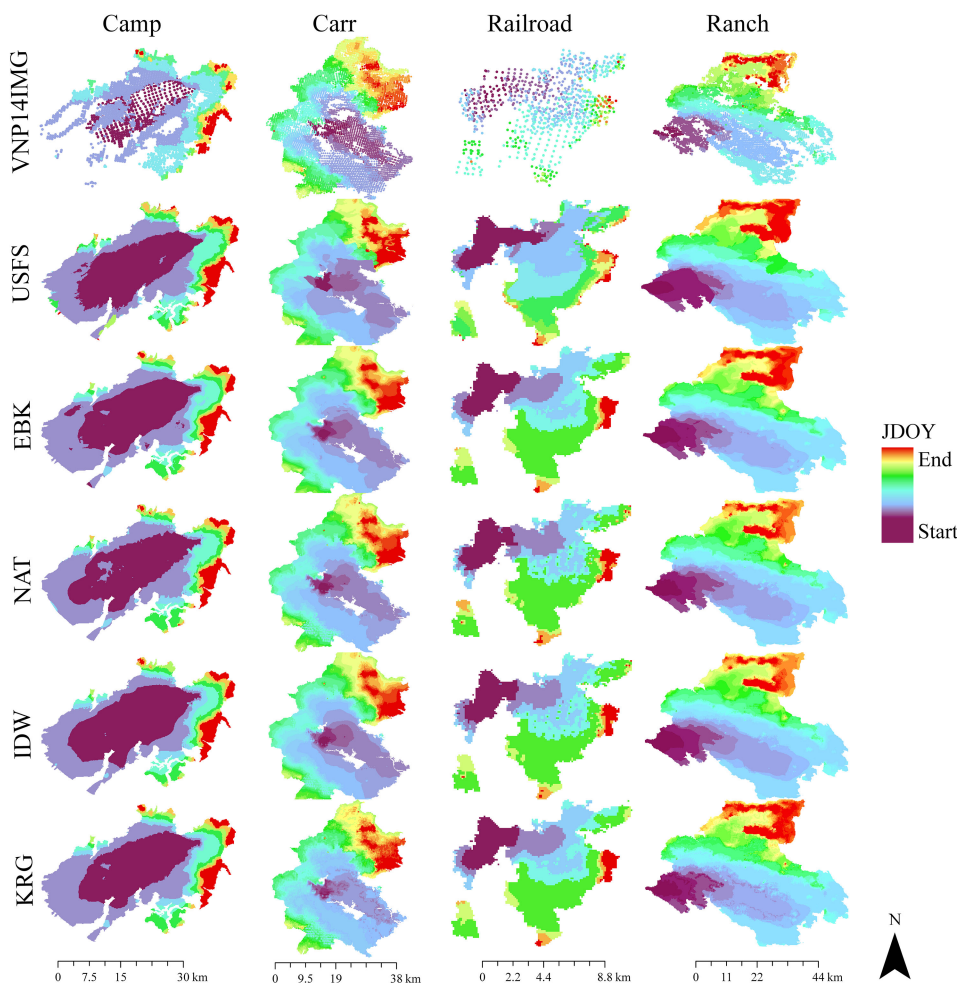


Fig. 4. Fire progression mapping with different interpolation techniques (from top to bottom) based on the VIIRS AF product in 2017 and 2018 for four individual fires: Camp, Carr, Railroad, and Ranch (from left to right).

of the VIIRS and resampled MODIS AF products achieved the highest proportion of daily matched area ( $0.35 \pm 0.11$ ) and cumulative matched area ( $0.84 \pm 0.12$ ), and the lowest proportion of daily false negative detections ( $0.23 \pm 0.11$ ) (see Table II and Fig. 3).

### B. Evaluation of Interpolated Daily Fire Perimeters: Temporal Dynamics

Similar to the dynamic observed from the USFS daily fire perimeters, the interpolated surfaces based on the AF products were able to capture the direction and rate of fire progression over the entire course of an individual fire (see Figs. 4 and 9). For example, when looking at Campfire, both VIIRS and MODIS missed the consistent fire hotspots in southwestern during the first two days of fire spread (see Fig. 2) but all models were able to resolve this underestimate and produce a smooth and continuous interpolated surface. The agreement between daily burned areas and the reference data was significantly improved from the interpolation (see Fig. 9), with an  $R^2$  of 0.99 and an

RMSE of 1.18 thousand acres for the Campfire when using VIIRS as input. Similar results were found for Carr, Railroad, and Ranch fires (see Fig. 4). Different models also existed certain differences in the interpolated fire perimeters. For example, those models derived from the original MODIS (1-km) during the first two days of rapid fire spread (see Fig. 9), the overestimate was particularly obvious in the IDW results.

Although the interpolated results of the Railroad fire captured the general direction and magnitude of fire progression, there still existed particular days and areas in which the estimated surfaces failed to match. The sporadic discontinuities, a phenomenon widely known as the bullseye effect, were a result of prolonged high-intensity flames that continued to burn during subsequent days, leading to the overlapping of AF detections (see Fig. 4). The accuracy results of the Railroad fire interpolated surfaces had a higher variation of model performance when assessing the sensitivity effect among different data input and model selection (see Fig. 4). In general, a relatively higher temporal accuracy was identified when using the combined layer as the input. For example, the  $R^2$  value of the natural neighbor

TABLE III  
TEMPORAL AND SPATIAL ACCURACY OF INTERPOLATED FIRE PROGRESSION MAPS

		Temporal Assessment				Spatial Agreement	
		Daily $R^2$	2-day Rolling $R^2$	Daily RMSE ( $10^3$ acres)	Rolling RMSE ( $10^3$ acres)	Kappa	Overall Accuracy
		Median $\pm$ AD*	Median $\pm$ AD	Median $\pm$ AD	Median $\pm$ AD	Median $\pm$ AD	Median $\pm$ AD
<b>Combination</b>	EBK	0.64 $\pm$ 0.39	0.83 $\pm$ 0.27	1.36 $\pm$ 1.35	0.73 $\pm$ 0.94	0.52 $\pm$ 0.15	0.57 $\pm$ 0.20
	IDW	0.64 $\pm$ 0.39	0.84 $\pm$ 0.26	1.34 $\pm$ 1.39	0.74 $\pm$ 1.07	0.50 $\pm$ 0.15	0.56 $\pm$ 0.21
	KRG	0.69 $\pm$ 0.38	0.84 $\pm$ 0.23	1.44 $\pm$ 1.31	0.80 $\pm$ 0.92	0.50 $\pm$ 0.14	0.56 $\pm$ 0.20
	NAT	0.70 $\pm$ 0.31	0.83 $\pm$ 0.20	1.25 $\pm$ 1.21	0.74 $\pm$ 0.94	0.51 $\pm$ 0.14	0.57 $\pm$ 0.20
<b>MODIS (1-km)</b>	EBK	0.26 $\pm$ 0.72	0.49 $\pm$ 0.63	1.71 $\pm$ 1.36	0.87 $\pm$ 0.80	0.45 $\pm$ 0.16	0.52 $\pm$ 0.22
	IDW	0.34 $\pm$ 0.67	0.63 $\pm$ 0.58	1.60 $\pm$ 1.33	0.94 $\pm$ 0.89	0.43 $\pm$ 0.16	0.51 $\pm$ 0.23
	KRG	0.24 $\pm$ 0.86	0.62 $\pm$ 0.54	1.52 $\pm$ 1.38	0.86 $\pm$ 0.89	0.45 $\pm$ 0.15	0.52 $\pm$ 0.22
	NAT	0.47 $\pm$ 0.51	0.70 $\pm$ 0.62	1.42 $\pm$ 1.03	0.86 $\pm$ 0.73	0.48 $\pm$ 0.15	0.54 $\pm$ 0.22
<b>MODIS (375-m)</b>	EBK	0.62 $\pm$ 0.37	0.68 $\pm$ 0.27	1.69 $\pm$ 1.19	0.98 $\pm$ 0.82	0.39 $\pm$ 0.13	0.48 $\pm$ 0.22
	IDW	0.52 $\pm$ 0.44	0.64 $\pm$ 0.70	1.50 $\pm$ 1.60	1.04 $\pm$ 1.21	0.41 $\pm$ 0.15	0.50 $\pm$ 0.24
	KRG	0.66 $\pm$ 0.37	0.70 $\pm$ 0.25	1.56 $\pm$ 1.27	0.91 $\pm$ 0.92	0.42 $\pm$ 0.15	0.50 $\pm$ 0.24
	NAT	0.62 $\pm$ 0.30	0.74 $\pm$ 0.22	1.38 $\pm$ 1.22	0.90 $\pm$ 0.96	0.44 $\pm$ 0.16	0.52 $\pm$ 0.23
<b>VIIRS</b>	EBK	0.54 $\pm$ 0.36	0.72 $\pm$ 0.26	1.31 $\pm$ 1.37	0.76 $\pm$ 0.99	0.53 $\pm$ 0.16	0.58 $\pm$ 0.19
	IDW	0.62 $\pm$ 0.41	0.77 $\pm$ 0.28	1.40 $\pm$ 1.37	0.73 $\pm$ 1.10	0.51 $\pm$ 0.16	0.56 $\pm$ 0.21
	KRG	0.57 $\pm$ 0.35	0.76 $\pm$ 0.31	1.36 $\pm$ 1.41	0.82 $\pm$ 1.00	0.52 $\pm$ 0.15	0.57 $\pm$ 0.19
	NAT	0.63 $\pm$ 0.30	0.78 $\pm$ 0.23	1.19 $\pm$ 1.27	0.70 $\pm$ 1.00	0.55 $\pm$ 0.15	0.59 $\pm$ 0.19

\*AD refers to the absolute deviation.

model using the combined VIIRS and MODIS layer was 0.76 but decreased to be 0.6 and 0.2 when using VIIRS, and MODIS AF as individual inputs.

By assessing the performance of fire incidents with exceptionally higher durations ( $>40$  days) and burned areas ( $>200,000$  acres), both Carr and Ranch fires generally agreed well with the USFS fire perimeter reference (Figs. 4 and 9). The estimated progression captured fire behaviors with patterns of rapid expansion followed by quick slowdowns, regardless of the method or input type. However, we also observed some outliers of abrupt fluctuations, which should be a more gradual progression that typically spread out a day or two during the reported time period.

With a comparison over all 42 large fires, the natural neighbor (NAT) method achieved the best performance in general with the higher  $R^2$  and lower RMSE values, regardless of the AF layers used as the input (see Table III and Fig. 5). For example, when using the VIIRS AF points as the input, it resulted in  $R^2$  of  $0.63 \pm 0.3$  and RMSE of  $1.19 \pm 1.27$  thousand acres, and only ten fires had  $R^2$  values below 0.36 (lower quartile) (see Fig. 5). IDW also achieved comparable performance for most fires  $R^2$  of  $0.62 \pm 0.41$  and RMSE of  $1.4 \pm 1.37$  but exhibited larger variations across the  $R^2$  values, with a decrease in the model performance for a greater number of fires relative to NAT.

When comparing the daily burned area estimates from different AF input layers with the USFS reference data, we found that the interpolation using the combined MODIS and VIIRS AF data

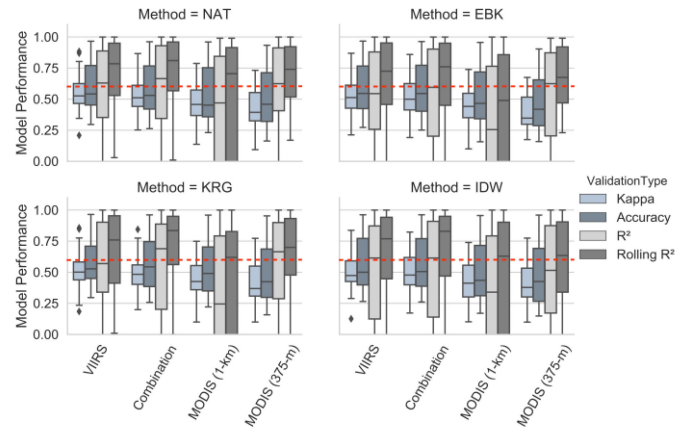


Fig. 5. Accuracy assessment of the model performance with different interpolation techniques and input AF layers for all 42 fires in the study area. The dashed red line is located at  $y = 0.6$  as a comparison basis.

yielded better performance in capturing temporal dynamics. For example, for the NAT interpolation method across all 42 fires, compared with  $R^2$  of  $0.47 \pm 0.51$  when using the MODIS 1 km AF and  $0.63 \pm 0.3$  when using the VIIRS AF,  $R^2$  increased to  $0.7 \pm 0.31$  when using the combined layer (see Table III). The RMSE values decreased slightly with the combined input. Similar results were also found for EBK and IDW methods. The

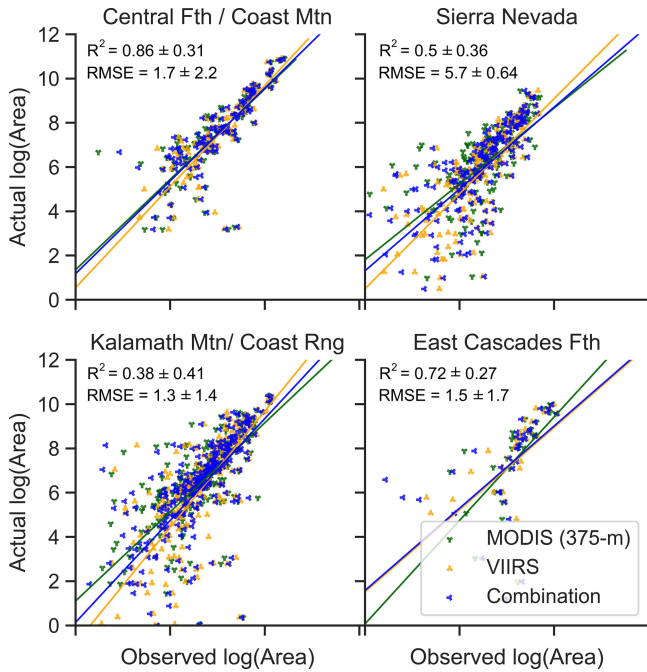


Fig. 6. Comparison of model performance plotting actual versus observed daily log of the total area burned with the corresponding median  $R^2$  and RMSE values for all 42 fires grouped by their respective ecoregions.

largest biases were found when using the original MODIS AF points at 1-km resolution as the input for the interpolation in terms of all methods, as shown by the lower  $R^2$  with a greater variation among fires and a higher RMSE (see Table III and Fig. 5). Considerable discrepancies could be found between the estimated burned acres from the MODIS 1-km AF product when it was compared with the USFS daily perimeters, especially for Carr and Railroad fires (see Fig. 9). However, by resampling the original MODIS AF input layer to 375 m as the input led to a significant improvement of the daily burned area estimation (see Fig. 5), especially for EBK, KRG, and IDW methods with an  $R^2$  ranging from  $0.52 \pm 0.44$  to  $0.66 \pm 0.37$  (see Table III). Additionally, we also identified that interpolations based on the VIIRS AF product typically yielded much higher accuracy than those from the MODIS 1 km AF product, and also had slight improvements compared with those based on the resampled MODIS-AF products for IDW and NAT at a daily temporal scale.

When assessed using a two-day moving window, the interpolated fire progression achieved a better agreement with the USFS reference than the daily progression, for all methods and all input layers. For example, the IDW interpolation method increased its  $R^2$  from  $0.64 \pm 0.39$  to  $0.84 \pm 0.26$  and decreased its RMSE from  $1.34 \pm 1.39$  to  $0.74 \pm 1.07$  (see Table III).

### C. Spatial Assessment

The difference map between the satellite-derived and USFS detection days was used to evaluate the spatial alignment of the interpolated surface and USFS perimeters. The total proportion of matching days across all fires was greater than 50% among

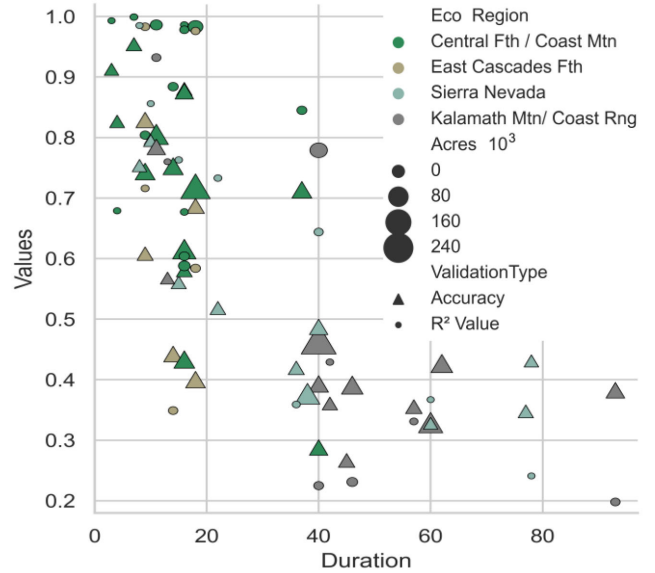


Fig. 7. Influence of the fire duration on model performance, quantified by  $R^2$  and accuracy values. Experimental results from the natural neighbor model using VIIRS AF as the input. The symbol hue is based on ecoregion, while the size is proportional to the area burned.

TABLE IV  
SPATIAL ALIGNMENT OF INTERPOLATED SURFACES AND USFS PERIMETERS AT DAILY TEMPORAL SCALE

Model	Combined (%)				VIIRS (%)				MODIS (%)			
	0	$\pm 1$	$\pm 2$	$\pm n$	0	$\pm 1$	$\pm 2$	$\pm n$	0	$\pm 1$	$\pm 2$	$\pm n$
EBK	55	30	10	5	61	26	9	5	45	31	14	10
IDW	54	30	10	5	58	28	9	5	47	31	13	9
KRG	52	31	11	6	58	28	9	5	46	30	14	10
NAT	55	28	10	6	61	25	9	5	50	29	12	9

The percentages were summarized over all fires and fire duration days based on the pixel-based map-to-map comparison, across all layers (columns) and methods (rows). The difference between the derived and USFS detection days was calculated for each pixel, e.g., 0 means exactly matching, while  $\pm 1$  day means one day before or after the reported time.

all combinations of methods when using VIIRS or the combined layer as the input. An additional 20%–30% was accounted for within  $\pm 1$  day of the USFS reported day. The VIIRS AF inputs led to the greatest proportions of matched days than any other input across all models, i.e.,  $\sim 60\%$  for exactly matching and  $\sim 86\%$  within  $\pm 1$  day, while the MODIS 1 km AF input led to a lower agreement (i.e., 10% lower in general) (see Table IV).

The pixel-based map-to-map evaluation through the confusion matrix, using the randomly selected USFS samples for reference, showed that all interpolation methods achieved an overall accuracy of  $57\% \pm 20\%$  when using the combined MODIS and VIIRS AF as the input, with a kappa score of  $0.50 \pm 0.15$  suggesting a weak-to-moderate spatial agreement (see Table III). Spatially, the results with the VIIRS AF input were similar to those from the combined layer across all methods, while the results from the MODIS 1 km AF were slightly less

TABLE V  
FIRE CHARACTERISTICS AND BIOPHYSICAL WEIGHTED AVERAGES FOR  
FIRE EVENTS ACROSS ECOREGIONS

Region	Fire Count	Duration (days)		Size (10 <sup>3</sup> acres)		Elevation (m <sup>2</sup> )
		Total	Mean	Total	Mean ± SD	Mean ± SD
Central Fth / Coast	14	223	15.93	671.89	47.99 ± 39.56	47.79 ± 33.06
Cascades Fth	6	79	13.17	179.34	29.89 ± 14.40	150.13 ± 30.91
Klamath Mtn	12	568	47.33	1044.1	87.01 ± 117.89	105.76 ± 30.38
Sierra Nevada	10	3844	38.40	224.64	22.46 ± 27.58	204.0 ± 36.14

\*SD refers to the standard deviation.

accurate. The NAT method performed slightly better when using MODIS AF as the input.

#### D. Comparison by Fire Characteristics

Among the four major ecoregions in this study area, the fire progression mapping yielded the best performance in the Central Foothills/Coastal Mountains, with the median  $R^2$  values of consistently higher than 0.8 and overall accuracy of spatial alignment greater than 70% across all interpolation approaches and input AF-data layers (see Fig. 6). In contrast, the fire progression maps with a lower agreement (i.e., Piers, Orleans, Eclipse, and Lions) were mostly located in the Klamath mountain/coastal range and Sierra Nevada ecoregions. For example, in terms of the median values for the NAT model with the combined layer as the input in the Klamath Mountain ecoregion, we observed a relatively low  $R^2$  of  $0.38 \pm 0.41$  and an accuracy rate of 39%. The interpolation for the East Cascades Foothill achieved a moderate accuracy, even with only six large fires during the study period.

We found that as the fire duration increased, the estimation accuracy of the daily area burned for an individual fire decreased (see Fig. 7). The majority of fires lasted less than 20 days (22 out of 42), for example, the daily areas estimated by the natural neighbor approach with VIIRS AF data explained more than 78% ( $R^2$ ) of daily variance compared with the USFS perimeter reference (e.g., Adobe, County, and Tubbs fires). Fires in Central Foothills/Coastal Mountains and East Cascades Foothill typically lasted shorter than those in the Klamath mountain/Coastal range and Sierra Nevada (see Table V and Fig. 6), which might be able to partly explain their better performance.

We also found that exceptionally large fires with longer durations did relatively well in comparison with smaller fires with similar duration times. For example, fires lasting longer than 40 days and burning over 200 000 acres, such as Mendocino Complex Ranch and Carr fires, achieved  $R^2$  values consistently higher than 0.65 (see Fig. 7). The increased model performance for larger fires may be due to the sensors ability to detect consistent and high-intensity burns.

## IV. DISCUSSION

Differences between the interpretations of fire incidences from satellite and airborne-based detections can also produce potential inherent biases for the comparison. Due to the intended

objectives of NIROPS, the fire perimeters record the largest extent of fire spread from the ignition, spanning across the areas that may not have yet been completely burnt. In contrast, AF products detect the pixel-level changes of thermal signals based on the algorithmically predetermined thresholds during overpass times. Therefore, the satellite-based fire detection can often have discrepancies of unburned and/or already burned areas, compared with the USFS perimeters. Moreover, uncertainties were also noticed in the USFS fire perimeter layers, including the over and under generalization of fire boundaries.

We also recognized that there are several factors affecting the accuracy of daily fire perimeter estimation from the discrete AF products derived from satellite observations. The limitations of sensors and platforms contributed to the uncertainties in the AF detection itself, although MODIS and VIIRS empower the advantage of frequent temporal scales, providing multiple overpasses per day. In this study, the AF points detected by MODIS and VIIRS were represented by a fixed size, e.g., 1 km and 375 m grids, as input layers. However, some artificial gaps seemed to still exist for adjacent AF points acquired during the same scan, due to the larger pixel size with the increasing scan angles. Further studies are needed to better handle [46], while preprocessing steps have been implemented to minimize the off-nadir pixel size variability in the most recent AF products [19], [24], and the spatial interpolation presented by this study helped to reduce those artificial gap issues.

Additionally, both MODIS and VAFPs filter out pixels contaminated with partial cloud cover, water, and invalid data, using the multispectral data [47]. Depending on the fire conditions and satellite's overpassing time, the significant omission error can be caused by the heavy cloud and/or smoke cover, dense tree canopy areas as well as during fires with rapid spread or low-intensity flames [34]. Topographic effects and landscape heterogeneity also contributed to the biases of fire progression mapping, for example, small fires over the areas with steep slopes, or rugged terrain, increased the challenge of the satellite-based detection [10]. Understory burning that occurs in forested terrains, such as the Sierra Nevada and Klamath mountain ecoregions will have a lower probability of detection due to the limited coverage of observations.

Smaller and cooler fires are typically harder to detect. Recent improvements in the subpixel fire detection have been made by taking advantage of the VIIRS night-time images at the panchromatic day-night band [47] and the shortwave IR band centered at 1.6- $\mu\text{m}$  (M10) [48]. At low light conditions without solar input, the high-radiant emissions in pixels containing the combustion sources lead to detectable anomalies in these bands. Future studies to further incorporate these additional night-time fire products, for example, the nocturnal hotspots detected by the firelight detection algorithm [47] and NOAA's VIIRS night fire product [48], are expected to increase the accuracy of daily fire progression mapping.

The fire progression estimation can be greatly improved by refining its spatial and temporal resolutions. Daytime and nighttime data from satellites with higher spatial resolution, such as Landsat-8 operational land imager, can be integrated to

enhance the fidelity of fire mapping and/or used for validation purposes [49], while opportunities presented from unmanned aerial vehicles (UAVs) for the forest and fire management have also been examined for its flexibility in capturing the real-time fire detection and behavior information from its very high spatial resolution [42], [50]. However, collecting and processing continuous aerial images of AFs over large extents are still inherent challenges for UAV-based data collection methods.

Additional improvements of interpolation methods for mapping daily or even hourly fire spread can be made by adding explanatory variables to inform the interpolation about the impacts of localized terrain and weather characteristics. For example, the interaction among the wind, slope, and fire is undoubtedly evident from a wide collection of fire spread observations [43]. However, currently, the gridded wind data are only available at a very coarse resolution. When considering the convergence of various drivers of fire spread, methods, such as EBK and cokriging, have the potential for incorporating localized variabilities.

The method presented in this study can be used to generate a large geodatabase for continuous daily fire spread, based on previously detected hotspots, and thus improve our understanding and modeling of fire behavior. When applied to the ongoing fires, the latency can be a few hours or half-day. For guidance on the fire suppression or firefighting strategies, near real-time and/or predicted information is needed. The high temporal frequency observations from geosynchronous weather monitoring instruments, such as the advanced baseline imager ABI onboard NOAA's geostationary operational environmental satellites (GOES) series, are extremely helpful to capture the fast-moving fires, providing near real-time detection capability [51]. The GOES-R series, for example, provides level-2 fire detection and characterization products at nominal 2-km resolution every 5–15 min [52], [53]. The integration of these multiscale observations and products from multiple sensors will improve our capability to detect wildfires, and map hourly and daily fire spread in the future.

## V. CONCLUSION

An accurate and timely method of mapping fire spread is needed to provide a crucial decision support for on-field fire-fighting efforts, and a large consistent daily fire progression database is critical for forest management strategies. We here examined the accuracy of a few spatial interpolation techniques to produce continuous daily fire progression maps at 375 m gridded resolution, from the discrete MODIS, VIIRS, and combined AF point products. The daily fire progression estimation with the natural neighbor method and the combined AF layer as the input performed comparatively well in terms of the temporal accuracy with an  $R^2$  of  $0.7 \pm 0.38$ , rolling  $R^2$  of  $0.83 \pm 0.25$ , RMSE of  $1.25 \pm 1.7$  thousand acres, and rolling RMSE of  $0.74 \pm 1.52$  (see Table III). The increase in model performance by incorporating a combination layer could be explained by the inherent improvements of both temporal and spatial resolutions from combining the two sensors. Additionally, the natural neighbor method using the VIIRS AF product achieved better performance with a kappa

score of 0.55 and an overall accuracy score of 0.59 (see Table III). The pixel-based comparison could explain 61% variability of the model performance in terms of the exact same day matching, and an additional 25% variability in terms of  $\pm 1$  day matching (see Fig. 5).

We also did a comprehensive assessment of the standard AF products from MODIS, VIIRS, and combined AF layers in quantifying and estimating the fire spread at a daily temporal interval over ecologically diverse California. Both MODIS and VAFPs detected AF fronts during their respective overpass times and accounted for comparable percentages of daily matched areas ( $<30\%$ ), based on the proportion of matching areas with reported USFS fire perimeters (see Table II). The combined MODIS and VIIRS layer achieved the highest proportion of both daily and cumulative matched areas as well as the lowest number of daily false negative detections. Overall, we found that the spatial interpolation reduced the omission errors in the standard satellite-based discrete hotspot detections.

By interpreting the performance of different approaches, this study contributed to the improvement of fire progression mapping at local to regional scales. Fire progression maps at daily timestamps allow for dynamic analysis of fire events, rather than relying on fixed perimeters from entire fire events at the end of the fire duration. The automatic workflow for generating reliable continuous fire perimeters, without relying on very limited aerial-based IR imagery, increases the accessibility and the availability of large spatial, and temporal data sets on daily fire behavior. This will further aid in the historical analysis of environmental controls (i.e., fuel, meteorological, topographical human-related variables) in fire spread, bottom-up carbon emissions estimation, and predictive fire behavior models [54], [55].

## APPENDIX

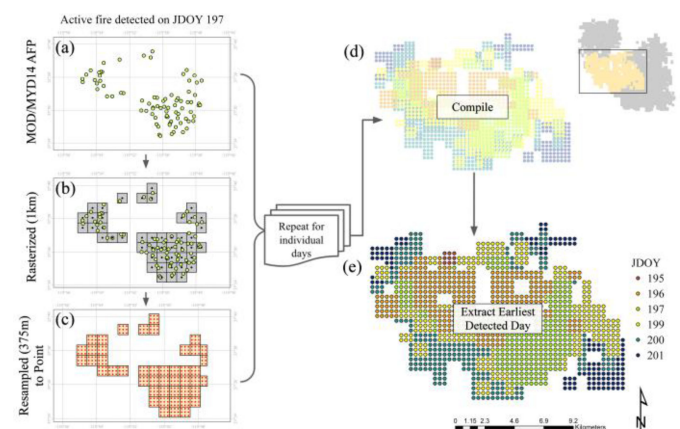


Fig. 8. Resampling workflow for MOD/MYD14 AF points illustrated for a subset of the Ferguson fire. (a) AF points for one of the fire days (e.g., JDOY 197), (b) rasterized to 1 km grids, and (c) Resampled to 375 m grids. This rasterization and resampling process was repeated for each unique day of a fire event, resulting in multiple layers, each with the grid values corresponding to JDOY. These layers were combined (d) into a single raster to represent all AF grids and (e) with corresponding JDOYs of burn. The earliest day of detection was prioritized for the grids with overlapping fire days.

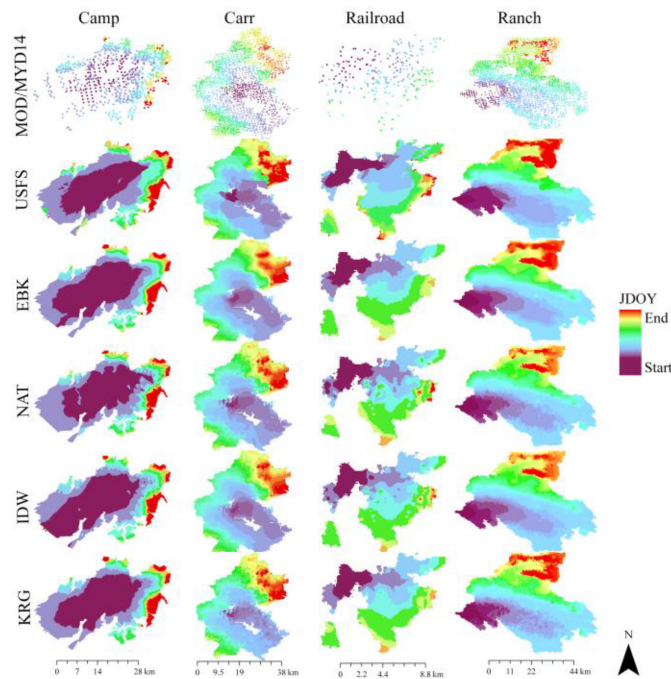


Fig. 9. Maps of continuous fire progression using different interpolation techniques (rows) based on the MODIS (1 km) AF product in 2017 and 2018 for four individual fires: Camp, Carr, Railroad, and Ranch (from left to right). The USFS fire incident perimeters as well as the MODIS AF points are also shown within the first two rows.

## REFERENCES

- [1] S. L. Stephens, R. E. Martin, and N. E. Clinton, "Prehistoric fire area and emissions from California's forests, woodlands, shrublands, and grasslands," *Forest Ecol. Manage.*, vol. 251, no. 3, pp. 205–216, 2007.
- [2] A. L. Westerling, H. G. Hidalgo, D. R. Cayan, and T. W. Swetnam, "Warming and earlier spring increase western US forest wildfire activity," *Science*, vol. 313, pp. 940–943, 2006.
- [3] J. T. Abatzoglou and A. P. Williams, "Impact of anthropogenic climate change on wildfire across western US forests," *Proc. Nat. Acad. Sci. USA*, vol. 113, no. 42, pp. 11770–11775, 2016.
- [4] J. K. Balch, B. A. Bradley, J. T. Abatzoglou, R. C. Nagy, E. J. Fusco, and A. L. Mahood, "Human-started wildfires expand the fire niche across the united states," *Proc. Nat. Acad. Sci. USA*, vol. 114, no. 11, pp. 2946–2951, 2017.
- [5] T. Schoennagel, M. G. Turner, and W. H. Romme, "Influence of fire interval and serotiny on postfire lodgepole pine density in Yellowstone National Park," *Ecology*, vol. 84, pp. 2967–2978, 2003.
- [6] S. L. Stephens *et al.*, "Drought, tree mortality, and wildfire in forests adapted to frequent fire," *Bio Science*, vol. 68, no. 2, pp. 77–88, 2018.
- [7] P. H. Greenfield, W. Smith, and D. C. Chamberlain, "Phoenix—The new forest service airborne infrared fire detection and mapping system," 2003. [Online]. Available: [https://fsapps.nwccg.gov/nirops/docs/upload/Phoenix\\_FS\\_Airborne\\_IR\\_Detection\\_Mapping.pdf](https://fsapps.nwccg.gov/nirops/docs/upload/Phoenix_FS_Airborne_IR_Detection_Mapping.pdf)
- [8] B. M. Collins, M. Kelly, J. W. van Wagtenonk, and S. L. Stephens, "Spatial patterns of large natural fires in Sierra Nevada wilderness areas," *Landscape Ecol.*, vol. 22, pp. 545–557, 2007.
- [9] J. R. Thompson and T. A. Spies, "Factors associated with crown damage following recurring mixed-severity wildfires and post-fire management in southwestern Oregon," *Landscape Ecol.*, vol. 25, pp. 775–789, 2010.
- [10] W. Schroeder *et al.*, "Integrated active fire retrievals and biomass burning emissions using complementary near-coincident ground, airborne and spaceborne sensor data," *Remote Sens. Environ.*, vol. 140, pp. 719–730, 2014.
- [11] A. K. Mebust, A. R. Russell, R. C. Hudman, L. C. Valin, and R. C. Cohen, "Characterization of wildfire NO<sub>x</sub> emissions using MODIS fire radiative power and OMI tropospheric NO<sub>2</sub> columns," *Atmos. Chem. Phys.*, vol. 11, no. 12, pp. 5839–5851, 2011.
- [12] D. Fornacca, G. Ren, and W. Xiao, "Performance of three MODIS fire products (MCD45A1, MCD64A1, MCD14ML), and ESA fire\_CCI in a mountainous area of northwest Yunnan, China, characterized by frequent small fires," *Remote Sens.*, vol. 9, no. 11, 2017, Art. no. 1131.
- [13] Y. J. Kaufman *et al.*, "Potential global fire monitoring from EOS-MODIS," *J. Geophys. Res. Atmos.*, vol. 103, no. D24, pp. 32215–32238, 1998.
- [14] L. Giglio, J. D. Kendall, and C. O. Justice, "Evaluation of global fire detection algorithms using simulated AVHRR infrared data," *Int. J. Remote Sens.*, vol. 20, no. 10, pp. 1947–1985, 1999.
- [15] L. Giglio, J. Desloires, C. O. Justice, and Y. J. Kaufman, "An enhanced contextual fire detection algorithm for MODIS," *Remote Sens. Environ.*, vol. 87, no. 2/3, pp. 273–282, 2003.
- [16] J. M. Lobert and J. Warnatz, "Emissions from combustion processes in vegetation," *Environ. Sci. Res. Rep.*, vol. 13, 1993.
- [17] C. O. Justice *et al.*, "The MODIS fire products," *Remote Sens. Environ.*, vol. 83, no. 1/2, pp. 244–262, 2002.
- [18] L. Giglio, W. Schroeder, and C. O. Justice, "The collection 6 MODIS active fire detection algorithm and fire products," *Remote Sens. Environ.*, vol. 178, pp. 31–41, 2016.
- [19] L. Giglio, L. Boschetti, D. P. Roy, M. L. Humber, and C. O. Justice, "The Collection 6 MODIS burned area mapping algorithm and product," *Remote Sens. Environ.*, vol. 217, pp. 72–85, 2018.
- [20] L. Giglio, T. Loboda, D. P. Roy, B. Quayle, and C. O. Justice, "An active-fire based burned area mapping algorithm for the MODIS sensor," *Remote Sens. Environ.*, vol. 113, pp. 408–420, 2009.
- [21] L. Boschetti, D. P. Roy, L. Giglio, H. Huang, M. Zubkova, and M. L. Humber, "Global validation of the collection 6 MODIS burned area product," *Remote Sens. Environ.*, vol. 235, 2019, Art. no. 111490.
- [22] R. E. Wolfe, J. C. Tilton, A. R. Isaacman, M. Nishihama, G. Lin, and K. P. Tewari, "Suomi NPP VIIRS prelaunch and on-orbit geometric calibration and characterization," *J. Geophys. Res., Atmos.*, vol. 118, no. 20, pp. 11508–11521, 2013.
- [23] I. Csizsar *et al.*, "Active fires from the Suomi NPP visible infrared imaging radiometer suite: Product status and first evaluation results," *J. Geophys. Res., Atmos.*, vol. 119, no. 2, pp. 803–816, 2014.
- [24] W. Schroeder, P. Oliva, L. Giglio, and I. A. Csizsar, "The new VIIRS 375m active fire detection data product: Algorithm description and initial assessment," *Remote Sens. Environ.*, vol. 143, pp. 85–96, 2014.
- [25] P. H. Freeborn, M. J. Wooster, D. P. Roy, and M. A. Cochrane, "Quantification of MODIS fire radiative power (FRP) measurement uncertainty for use in satellite-based active fire characterization and biomass burning estimation," *Geophys. Res. Lett.*, vol. 41, no. 6, pp. 1988–1994, 2014.
- [26] T. N. Polivka, E. J. Hyer, J. Wang, and D. A. Peterson, "First global analysis of saturation artifacts in the VIIRS infrared channels and the effects of sample aggregation," *IEEE Geosci. Remote Sens. Lett.*, vol. 12, no. 6, pp. 1262–1266, Jun. 2015.
- [27] Fire Information for Resource Management System (FIRMS), 2020. [Online]. Available: <https://earthdata.nasa.gov/earth-observation-data/near-real-time/firms>
- [28] D. K. Davies, S. Ilavajhala, M. M. Wong, and C. O. Justice, "Fire information for resource management system: Archiving and distributing MODIS active fire data," *IEEE Trans. Geosci. Remote Sens.*, vol. 47, no. 1, pp. 72–79, Jan. 2009.
- [29] S. A. Parks, "Mapping day-of-burning with coarse-resolution satellite fire-detection data," *Int. J. Wildland Fire*, vol. 23, no. 2, pp. 215–22, 2014.
- [30] S. Veraverbeke, F. Sedano, S. J. Hook, J. T. Randerson, Y. Jin, and B. M. Rogers, "Mapping the daily progression of large wildland fires using MODIS active fire data," *Int. J. Wildland Fire*, vol. 23, no. 5, pp. 655–667, 2014.
- [31] EPA, "Primary distinguishing characteristics of level III ecoregions of the continental united states," Website, 2013.
- [32] T. Griggs *et al.*, "Northern California fires have destroyed at least 5,700 buildings," *NY Times*, Oct. 14, 2017.
- [33] E. Baron and E. Baldassari, "Camp fires return home, some to devastation," *Mercury News*, Nov. 18, 2018.
- [34] I. A. Csizsar, J. T. Morissette, and L. Giglio, "Validation of active fire detection from moderate-resolution satellite sensors: The MODIS example in northern Eurasia," *IEEE Trans. Geosci. Remote Sens.*, vol. 44, no. 7, pp. 1757–1764, Jul. 2006.
- [35] P. Oliva and W. Schroeder, "Assessment of VIIRS 375m active fire detection product for direct burned area mapping," *Remote Sens. Environ.*, vol. 160, pp. 144–155, 2015.
- [36] R. Sibson, "A brief description of natural neighbor interpolation," in *Interpolating Multivariate Data*, V. Barnett Ed. Hoboken, NJ, USA: Wiley, 1981, pp. 21–36.

- [37] K. Krivoruchko, "Empirical Bayesian kriging implemented in ArcGIS geostatistical analyst," *ARCuser*, vol. 15, no. 4, pp. 6–10, 2012.
- [38] M. R. Holdaway, "Spatial modeling and interpolation of monthly temperature using kriging," *Climate Res.*, vol. 6, pp. 215–225, 1996.
- [39] A. C. Schwendel, I. C. Fuller, and R. G. Death, "Assessing DEM interpolation methods for effective representation of upland stream morphology for rapid appraisal of bed stability," *River Res. Appl.*, vol. 28, pp. 567–584, 2012.
- [40] C. Klauber *et al.*, "Use of ordinary kriging and Gaussian conditional simulation to interpolate airborne fire radiative energy density estimates," *Int. J. Wildland Fire*, vol. 27, no. 4, pp. 228–240, 2018.
- [41] V. P. Samsonova, Y. N. Blagoveshchenskii, and Y. L. Meshalkina, "Use of empirical Bayesian kriging for revealing heterogeneities in the distribution of organic carbon on agricultural lands," *Eurasian Soil Sci.*, vol. 50, no. 3, pp. 305–311, 2017.
- [42] G. D. Papadopoulos and F.-N. Pavlidou, "A comparative review on wildfire simulators," *IEEE Syst. J.*, vol. 5, no. 2, pp. 233–243, Jun. 2011.
- [43] R. Rothermel, "A mathematical model for predicting fire spread in wildland fuels," U.S. Dept. Agriculture, Intermountain Forest Range Experiment Station, Research Paper INT-115, 1972.
- [44] M. Fosberg, "Weather in wildland fire management: The fire weather index," in *Proc. Conf. Sierra Nevada Meteorol.*, 1978, pp. 1–4.
- [45] P. S. John, A. M. Phillips, J. Serna, S. Kohli, and L. Newberry, "California fire: What started as a tiny brush fire became the state's deadliest wildfire," 2018. [Online]. Available: [Latimes.com](https://www.latimes.com)
- [46] T. N. Polivka, J. Wang, L. T. Ellison, E. J. Hyer, and C. M. Ichoku, "Improving nocturnal fire detection with the VIIRS day–night band," *IEEE Trans. Geosci. Remote Sens.*, vol. 54, no. 9, pp. 5503–5519, Sep. 2016.
- [47] A. Sharma, J. Wang, and E. M. Lennartson, "Intercomparison of MODIS and VIIRS fire products in Khanty-Mansiysk Russia: Implications for characterizing gas flaring from space," *Atmosphere*, vol. 8, no. 6, 2017, Art. no. 95.
- [48] C. D. Elvidge, K. E. Baugh, F.-C. Hsu, and M. Zhizhin, "VIIRS nightfire: Satellite pyrometry at night," *Remote Sens.*, vol. 5, no. 9, pp. 4423–4449, 2013.
- [49] W. Schroeder, P. Oliva, L. Giglio, B. Quayle, E. Lorenz, and F. Morelli, "Active fire detection using Landsat-8/OLI data," *Remote Sens. Environ.*, vol. 185, pp. 210–220, 2016.
- [50] L. Zhang, B. Wang, W. Peng, C. Li, Z. Lu, and Y. Guo, "A method for forest fire detection using UAV," *Adv. Sci. Technol. Lett.*, vol. 81, pp. 69–74, 2015.
- [51] A. Koltunov, S. L. Ustin, B. Quayle, B. Schwind, V. G. Ambrosia, and W. Li, "The development and first validation of the GOES early fire detection (GOES-EFD) algorithm," *Remote Sens. Environ.*, vol. 184, pp. 436–453, 2016.
- [52] F. Li, X. Zhang, S. Kondragunta, C. C. Schmidt, and C. D. Holmes, "A preliminary evaluation of GOES-16 active fire product using Landsat-8 and VIIRS active fire data, and ground-based prescribed fire records," *Remote Sens. Environ.*, vol. 237, Feb. 2020, Art. no. 111600.
- [53] X. Zhang, S. Kondragunta, J. Ram, C. Schmidt, and H.-C. Huang, "Near-real-time global biomass burning emissions product from geostationary satellite constellation," *J. Geophys. Res., Atmos.*, vol. 117, 2012, Art. no. D14201.
- [54] L. Boschetti, C. O. Justice, D. P. Roy, and L. Giglio, "Global assessment of the temporal reporting accuracy and precision of the MODIS burned area product," *Int. J. Wildland Fire*, vol. 19, no. 6, pp. 705–709, 2010.
- [55] T. T. van Leeuwen and G. R. van der Werf, "Spatial and temporal variability in the ratio of trace gases emitted from biomass burning," *Atmos. Chem. Phys.*, vol. 11, no. 8, pp. 3611–3629, 2011.



**Erica Scaduto** received the B.S. degree in geographical science and environmental science and technology with a concentration in geographic information systems from the University of Maryland, College Park, MD, USA, in 2015. She is currently working toward the M.A. degree in geography with the University of California, Davis, Davis, CA, USA.

Her research interests include applications of remote sensing and geospatial science in ecological systems, specifically pertaining to wildfire and land cover/land use change.



**Bin Chen** received the B.S. degree in geographic information systems from Wuhan University, Wuhan, China, in 2013, and the Ph.D. degree in global environmental change from Beijing Normal University, Beijing, China, in 2017.

He is currently a Postdoctoral Researcher with the University of California, Davis, Davis, CA, USA. He has authored or coauthored more than 30 journal articles, including *Science*, *Remote Sensing of Environment*, *ISPRS Journal of Photogrammetry and Remote Sensing*, *IEEE TRANSACTIONS ON GEOSCIENCE AND*

*REMOTE SENSING*, etc. His research interests include most aspects of geoscience and remote sensing, specifically multisource data-model fusion and geospatial big data analysis in the field of agricultural, wildfire, and urban science.



**Yufang Jin** received the B.S. degree in atmospheric science and the M.S. degree in environmental science and management from Beijing University, Beijing, China, and the Ph.D. degree in geography from Boston University, Boston, MA, USA, in 1995, 1998, and 2002, respectively.

She is a Professor with the Department of Land, Air, and Water Resources, University of California, Davis, Davis, CA, USA. Her research focuses on terrestrial remote sensing, ecosystem dynamics, and big data for sustainable agricultural and natural resource management.